




Cite this: *RSC Adv.*, 2018, 8, 547

Manipulating catalytic activity and durability of Pt-modified Cu–Fe–La/ γ -Al₂O₃ ternary catalyst for catalytic wet air oxidation: effect of calcination temperature†

Yongli Zhang, * Yanbo Zhou, Qingyu Wang, Junjun Shi, Chao Peng, Lingfeng He and Liang Shi

A series of novel Pt-modified Cu–Fe–La/ γ -Al₂O₃ catalysts were prepared by an incipient-wetness impregnation method, and their performances were evaluated in catalytic wet air oxidation (CWAO) of printing and dyeing wastewater (PDW). The as-prepared catalysts were characterized by X-ray photoelectron spectroscopy (XPS), nitrogen adsorption–desorption, X-ray diffraction (XRD), field emission scanning electron microscopy (FESEM), transmission electron microscopy (TEM), Raman spectroscopy, and temperature programmed reduction by hydrogen (H₂-TPR). The effects of catalyst composition and calcination temperature on the catalytic performance were investigated. The chemical oxygen demand (COD) removal efficiency and decolorization rate are satisfactory over Cu_{1.5}Fe_{1.5}La₃/ γ -Al₂O₃ catalyst, with poor stability under CWAO conditions. In contrast, catalytic performance and stability of all Pt-modified catalysts are significantly improved. With increasing calcination temperatures from 350 °C to 750 °C, the activity of the catalysts significantly decreases from 97.3% to 84.6%, and the size of the particles varies from 4.71–6.95 nm. The XRD, HRTEM, and XPS results indicate that the Pt₁Cu₁Fe₁La₃/ γ -Al₂O₃ catalyst mostly comprises Pt, CuO, Fe₃O₄, and La₂O₃, and the incorporation of Pt increases the binding energies (BEs) of the metal elements in the catalyst, owing to synergistic interactions between the Pt and the Cu, Fe, and La elements. After five cycles, the COD removal efficiency and decolorization rate for PDW over the Pt₁Cu₁Fe₁La₃/ γ -Al₂O₃ catalyst calcined at 650 °C remain comparable with the fresh catalyst, indicating that Pt-modified Cu–Fe–La/ γ -Al₂O₃ ternary oxide is a promising catalyst with high activity and stability for CWAO treatment.

Received 29th October 2017
 Accepted 18th December 2017

DOI: 10.1039/c7ra11899f

rsc.li/rsc-advances

1 Introduction

The printing and dyeing wastewater (PDW) from the textile industry, printing industry, and dye production is a major source of organic pollutants with complex compositions, high concentration, and poor biodegradability,¹ harmful for water bodies and human health. A great many reports have documented that the conventional methods, such as physical and chemical methods,² biological degradation,³ and conventional chemical oxidation methods,⁴ couldn't effectively degrade refractory organic pollutants in PDW.⁵ Thus, it is vital to develop a new method to treat PDW in an effective way.

Catalytic wet air oxidation (CWAO) technology has advantages of high efficiency, low cost, and no secondary pollution. Thus, it has recently attracted considerable attention due to its

wide application in wastewater treatment and high efficiency in eliminating various types of pollutants.^{6–8} In order to optimize reaction conditions and improve the catalytic performance (*i.e.* high efficiency, good stability and reusability), lots of heterogeneous catalysts have been successfully prepared.^{9–11} In general, the heterogeneous materials, such as transition metals, rare-earth metals, and noble metals, are widely used as catalysts due to their superior physicochemical properties. Transition metals (*e.g.* Cu, Fe or Co) display high catalytic activity for treatment of organic wastewater and are less expensive,^{12–14} while they are relatively unstable. Rare-earth metals (*e.g.*, Ce or La) are known to improve the catalytic performance by changing the physical structure of the catalyst. Thus, they are widely used as additive agents.^{15,16} Noble metals, especially Pt-based catalysts, have been paid great attention and play as a crucial role in catalytic reaction, owing to high catalytic activity, long lifetimes, and applicability towards a wide range of substrates.^{17–19} Noble Pt-based catalysts have exhibited the excellent catalytic performance in the CWAO process of different model compounds as well as industrial wastewaters. Although Pt-based catalysts are

School of Environment and Chemical Engineering, Foshan University, Foshan, Guangdong, 528000, China. E-mail: yongli1929@fosu.edu.cn; Fax: +86-757-82781287; Tel: +86-757-82781287

† Electronic supplementary information (ESI) available. See DOI: 10.1039/c7ra11899f



resistant to the metal leaching upon most occasions, they still suffer from poisoning during CWAO process. Furthermore, the formation of carbon-containing deposits leads to a loss of catalytic activity. Therefore, both stability and catalytic activity of a CWAO catalyst should be assessed while considering its application in wastewater treatment.

Recently it has been recognized that addition of Pt nanoparticles (NPs) may affect the catalytic activity and stability of CWAO catalysts.^{20–22} Rocha *et al.*²³ reported that 5 wt% of Pt was impregnated in the TiO₂–Ce support prepared by sol–gel method, and the prepared catalyst exhibited an excellent catalytic efficiency with an optimal proportion (55%/45%) of Pt⁰/Pt²⁺, due to the higher oxygen storage capacity (OSC) on the catalyst surface, while the catalyst activity decreased with Pt²⁺ alone (100%). Pt has been proven to be intrinsically more active than Ru in Pt and Ru supported on TiO_{2–x} wt% CeO₂ for CWAO of phenol due to high OSC values and the presence of Lewis acid sites.²⁴ Lousteau *et al.*²⁵ investigated the different noble metals enhanced the activity in the CWAO of ammonia in this descending order: Pt > Pd > Ir > Ru > Rh. The oxygen coverage on surface of the Pt-based catalysts plays a significant role on both the activity and the selectivity. In addition, Pt dispersion is a decisive factor influencing the performance of CWAO catalysts in degradation of aniline²⁶ and phenol.²⁷ In conclusion, the catalytic activity of Pt-based catalysts is significantly affected by dispersion, chemical state and content of Pt. However, to the best of our knowledge, interactions between Pt and other active components are not well demonstrated, and CWAO performance of Pt-modified catalyst is not clearly linked with particle size, morphology and phase transformation of oxides at different calcination temperature.

In our previous study,²⁸ a heterogeneous Cu_{1.5}Fe_{1.5}La₃/γ-Al₂O₃ catalyst was successfully fabricated and used for the treatment of PDW. However, this new catalyst suffered from deactivation due to dissolution of the active components under the harsh reaction conditions in the CWAO process. These disadvantages motivate the research for improving stability and catalytic activity of Cu_{1.5}Fe_{1.5}La₃/γ-Al₂O₃ catalyst. The major objective of this study is to design and prepare highly active Pt-based ternary catalysts for CWAO treatment. In addition, in order to investigate the effects of particle size of as-prepared catalysts and synergistic effects among Pt and other metal catalysts, a series of novel Pt-doped Cu–Fe–La/γ-Al₂O₃ catalysts with different Pt contents were prepared, and the intrinsic activity and stability over these catalysts at different calcination temperatures were investigated.

2 Experimental

2.1 Catalyst preparation

All the chemicals used in this study were of analytical grade. For preparation of the γ-Al₂O₃ support, the pseudo-boehmite particles were washed thrice with distilled water, and then dried at 105 °C for 10 h with ventilation in an electro-thermal blow-drying oven. Finally, the sample was calcined at 650 °C (heating rate: 6 °C min^{–1}) for 3 h in a high-temperature heater case.

With the desired 6 wt% of total metal loading, the obtained samples were designated as Pt_xCu_(1.5–0.5x)Fe_(1.5–0.5x)La₃/γ-Al₂O₃,

where *x* and 1.5–0.5*x* indicate the weight percentage of Pt and transition metals (such as Cu and Fe) loading, respectively, and *x* varied in a range of 0, 0.5, 1.0, and 3.0. This means that the theoretical Pt loading was 0, 0.5, 1.0 or 3.0 wt%. The Pt_{*x*}Cu_(1.5–0.5*x*)Fe_(1.5–0.5*x*)La₃/γ-Al₂O₃ catalysts were prepared by the incipient-wetness impregnation method. Briefly, Pt(NO₃)₂ (18.15*x* g, 18.02%), Cu(NO₃)₂·3H₂O {(11.41–3.80*x*) g}, Fe(NO₃)₃·9H₂O {(21.70–7.23*x*) g}, and La(NO₃)₃·6H₂O (18.70 g) were dissolved in de-ionized water (148.19 + 7.12*x* g), and solutions of 200.00 g metal precursors and the solid support γ-Al₂O₃ of 150.00 g were mixed and dynamically impregnated for 12 h in an air-bath oscillator. The sample was then drained, and dried at 105 °C for 10 h with ventilation. The impregnation and drying processes were repeated twice. Finally, in a high-temperature heater case, the sample was calcined at the temperatures of 350–750 °C (at 100 °C intervals, heating rate of 6 °C min^{–1}) for 3 h, and then the final catalysts were sieved to obtain particles between 40 and 60 mesh. The Pt NPs size was manipulated by changing different sintering temperatures.

2.2 Catalyst characterization

The binding energies of the elements in the catalyst were determined using an X-ray photoelectron spectrometer (XPS, Kratos AXIS Ultra DLD, Shimadzu, Japan) using Al K α radiation. The specific surface area, pore volume, and pore diameter of the catalysts were determined using a physical adsorption instrument (ASAP2400, Micrometrics, USA) at –196 °C. The phase compositions of the catalysts were determined with X-ray diffraction (XRD) analysis, on a Bruker D8 Advance X-ray diffractometer (Cu K α radiation, 40 kV and 40 mA, Germany). The surface morphology and particle size distribution of the catalysts were recorded on a field emission scanning electron microscopy (FESEM, ZEISS Uriga FIB, Germany) and high-resolution transmission electron microscopy (HRTEM, FEI Tecnai G2, USA), respectively. The samples were crushed into a powder and dispersed in a small volume of ethanol under sonicating the mixture for 15 min, and deposition of the obtained suspensions onto a holey carbon TEM grid. Raman spectroscopy were recorded in a RENISHAW inVia Reflex Raman spectroscopy with an Ar-laser excitation wavelength of 514.5 nm, and data acquisition were done with the LabSpec (Jobin Yvon-Horiba) software. Temperature programmed reduction by hydrogen (H₂-TPR) experiments were carried out on a Micromeritics Autochem 2920 II instrument equipped with a thermal conductivity detector using the gas mixture (10 vol% H₂ in Ar) at a flow rate of 20 mL min^{–1}. The temperature increased from room temperature to 900 °C (10 °C min^{–1}). Prior to the H₂-TPR experiments, precisely weighted 20 mg catalyst was first pretreated at the corresponding calcination temperature for 1 h under the oxygen condition and then naturally cooled to room temperature with an Ar flow.

2.3 Catalyst performance evaluation and analytical method

To evaluate the CWAO performance of the catalyst samples, synthetic PDW containing methyl orange (MO) was prepared with a concentration of 951.6 mg L^{–1}, a COD of 2000 mg L^{–1},



and pH of 6.4. The degradation of PDW sample by CWAO was conducted in a reactor (Weihai, GS type, 0.5 L) dosed with the composite catalyst of 2 g L^{-1} , stirred at 500 rpm, and pressurized to an oxygen partial pressure of 2.0 MPa. Then the mixture was heated to $200 \text{ }^\circ\text{C}$ and 20 mL solution was sampled at specific time intervals (10, 20, 40, 60, and 90 min) during the reaction. To estimate the catalytic activity, the COD was measured by an opened reflux method. Briefly, the organic compounds were oxidized by potassium dichromate under acidic condition and at $160 \text{ }^\circ\text{C}$ for 2 h. Then the excessive potassium dichromate remaining in the solution was determined by titration with ferrous ammonium sulfate.²⁹ The COD removal efficiency for PDW was defined as eqn (1):

$$D (\%) = \frac{C_0 - C_t}{C_0} \times 100\% \quad (1)$$

where D is the COD removal efficiency of PDW, C_0 is the initial COD concentration of PDW, and C_t is its COD concentration at sampling time t .

In addition, the absorbance of each solution recording the absorbance at 465 nm was analyzed using a TU-1810 UV-Vis spectrophotometer. The catalytic stability was evaluated by monitoring the metal leaching by an inductively coupled plasma-atomic emission spectrometer (ICP-AES, 7700s, Agilent, USA).

3 Results and discussion

3.1 Effect of multi-metallic interactions

To investigate the effects of catalyst compositions on activity and stability, the performances of all the catalysts were evaluated in CWAO of PDW. Fig. 1 shows that for all the catalyst samples calcined at $650 \text{ }^\circ\text{C}$, COD removal efficiency and decolorization rate demonstrate a similar trend. The overall catalytic activity of all samples followed the order of $\text{Pt}_1\text{Cu}_1\text{Fe}_1\text{La}_3/\gamma\text{-Al}_2\text{O}_3$ (1.0 wt% Pt) > $\text{Pt}_{0.5}\text{Cu}_{1.25}\text{Fe}_{1.25}\text{La}_3/\gamma\text{-Al}_2\text{O}_3$ (0.5 wt% Pt) > $\text{Pt}_3\text{La}_3/\gamma\text{-Al}_2\text{O}_3$ (3.0 wt% Pt) > $\text{Cu}_{1.5}\text{Fe}_{1.5}\text{La}_3/\gamma\text{-Al}_2\text{O}_3$ > $\gamma\text{-Al}_2\text{O}_3$. Only 31.9% and 60.4% of COD removal efficiency and decolorization rate of the dye was removed in CWAO reaction with $\gamma\text{-Al}_2\text{O}_3$ alone, respectively. A decolorization of 98.9% for PDW can be achieved by $\text{Cu}_{1.5}\text{Fe}_{1.5}\text{La}_3/\gamma\text{-Al}_2\text{O}_3$, while the COD removal efficiency was only 68.9% at 90 min. Enhanced COD removal efficiency can be observed for the CWAO of PDW over the Pt-doped Cu-Fe-La/ γ -

Al_2O_3 catalysts. The COD removal efficiency and decolorization rate greatly increased to 94.7% and 99.5% over the $\text{Pt}_1\text{Cu}_1\text{Fe}_1\text{La}_3/\gamma\text{-Al}_2\text{O}_3$ (1.0 wt% Pt) catalyst, respectively.

The leaching of the metals, especially for the transition metals, is of great concern in CWAO processes. Thus, the stability of the $\text{Pt}_x\text{Cu}_{(1.5-0.5x)}\text{Fe}_{(1.5-0.5x)}\text{La}_3/\gamma\text{-Al}_2\text{O}_3$ ($x = 0, 0.5, 1.0$, and 3.0) catalysts were evaluated after the consecutive catalytic reactions. As shown in Fig. 1c, although the decolorization efficiency over $\text{Cu}_{1.5}\text{Fe}_{1.5}\text{La}_3/\gamma\text{-Al}_2\text{O}_3$ catalyst was satisfactory, its instability was severe under CWAO conditions: 4.05 mg L^{-1} of Cu, 2.10 mg L^{-1} of Fe and 0.28 mg L^{-1} of La was leached, respectively. In contrast, the release of active metals in all Pt-modified catalysts was remarkably reduced. Only a total of 1.32 mg L^{-1} of metals was dissolved in $\text{Pt}_1\text{Cu}_1\text{Fe}_1\text{La}_3/\gamma\text{-Al}_2\text{O}_3$ (1.0 wt% Pt). A significant synergetic effect between Pt and transition metals (such as Cu and Fe) should play a role in the enhancement of both the activity and stability of the catalysts.

To explore the structure/property relationships in Pt-based Cu-Fe-La/ $\gamma\text{-Al}_2\text{O}_3$ ternary catalyst, XPS analysis for the $\text{Pt}_1\text{Cu}_1\text{Fe}_1\text{La}_3/\gamma\text{-Al}_2\text{O}_3$ and $\text{Cu}_{1.5}\text{Fe}_{1.5}\text{La}_3/\gamma\text{-Al}_2\text{O}_3$ catalysts calcined at $650 \text{ }^\circ\text{C}$, was performed. As depicted in Fig. 2a, the spectra of two catalyst samples show the elements of Al, O, Cu, Fe, La, and C, whereas the C element was likely originated from external contamination. The Pt element could not be directly detected in the survey of the $\text{Pt}_1\text{Cu}_1\text{Fe}_1\text{La}_3/\gamma\text{-Al}_2\text{O}_3$ catalyst due to the partial overlapping of Al 2p and Pt 4f. The deconvolution of XPS peaks is shown in Fig. 2b. A strong peak with binding energy (BE) of 74.3 eV was attributed to Al 2p in the $\text{Cu}_{1.5}\text{Fe}_{1.5}\text{La}_3/\gamma\text{-Al}_2\text{O}_3$ catalyst, the BEs of 69.7 , 71.8 , and 72.3 eV were assigned to $4f_{7/2}$ of Pt, Pt^{2+} , and Pt^{4+} , respectively, but lower than the corresponding BEs of 70.7 , 73.3 and 74.1 eV reported by Kim *et al.*³⁰ Compared with the $\text{Cu}_{1.5}\text{Fe}_{1.5}\text{La}_3/\gamma\text{-Al}_2\text{O}_3$ catalyst, the peaks of O 1s for the Pt-modified catalyst were slightly shifted to the higher BEs. For the O 1s peaks of the $\text{Pt}_1\text{Cu}_1\text{Fe}_1\text{La}_3/\gamma\text{-Al}_2\text{O}_3$ catalyst, the BEs of 530.0 , 531.3 , and 532.5 eV were attributed to lattice oxygen denoted (O_L), surface adsorbed oxygen denoted (O_S), and hydroxyl or molecular water species denoted (O_H) (Fig. 2c), respectively. Based on the peak areas calculated from the O 1s spectrum, the percentage content of surface adsorbed oxygen ($\text{O}_S(\%) = S(\text{O}_S)/S(\text{O}_L + \text{O}_S + \text{O}_H)$) varied from 53.8% to 58.9%. According to the literature,³¹⁻³³ the catalytic activity has been remarkable increased with the increase of O_S . After

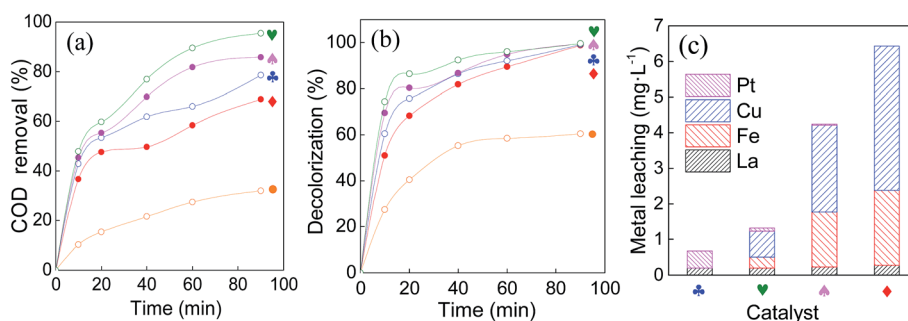


Fig. 1 Influence of components on the activity and stability of catalysts. (a) COD removal efficiency, (b) decolorization rate, (c) metal leaching, (♣) $\text{Pt}_3\text{La}_3/\gamma\text{-Al}_2\text{O}_3$, (♥) $\text{Pt}_1\text{Cu}_1\text{Fe}_1\text{La}_3/\gamma\text{-Al}_2\text{O}_3$, (♠) $\text{Pt}_{0.5}\text{Cu}_{1.25}\text{Fe}_{1.25}\text{La}_3/\gamma\text{-Al}_2\text{O}_3$, (◆) $\text{Cu}_{1.5}\text{Fe}_{1.5}\text{La}_3/\gamma\text{-Al}_2\text{O}_3$ and (●) $\gamma\text{-Al}_2\text{O}_3$.



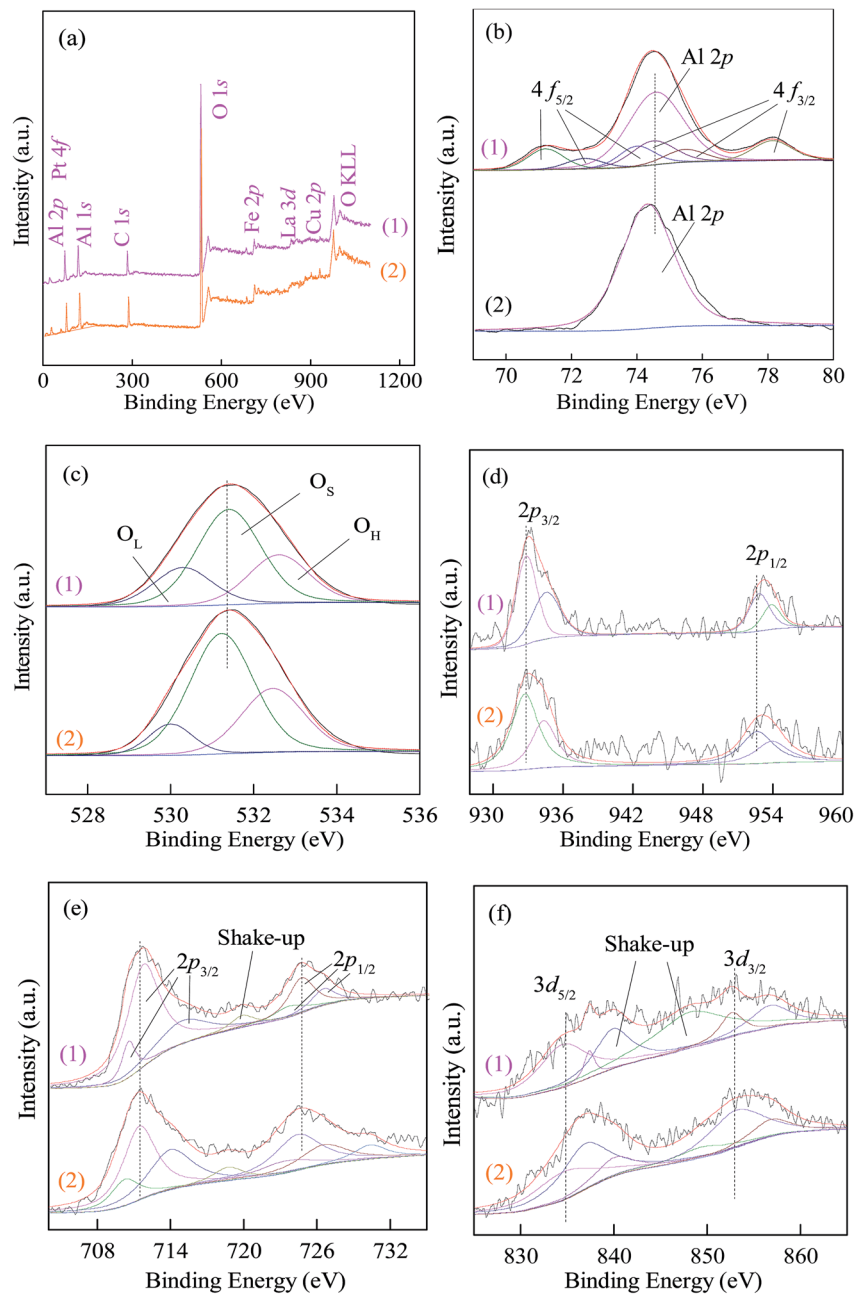


Fig. 2 XPS spectra for the elements of (1) $\text{Pt}_1\text{Cu}_1\text{Fe}_1\text{La}_3/\gamma\text{-Al}_2\text{O}_3$ catalyst and (2) $\text{Cu}_{1.5}\text{Fe}_{1.5}\text{La}_3/\gamma\text{-Al}_2\text{O}_3$ catalyst: (a) survey; (b) Pt 4f; (c) O 1s; (d) Cu 2p; (e) Fe 2p and (f) La 3d.

addition of Pt, the Cu $2p_{3/2}$ peaks of Cu^{2+} and Cu^+ were shifted from 932.2 and 933.7 eV to 932.9 and 934.6 eV (Fig. 2d). As shown in Fig. 2e, the peaks Fe $2p_{3/2}$ for Fe^{3+} (726.4 eV), Fe_3O_4 (724.4 eV), Fe^{2+} (723.4 eV), and satellite peak (718.7 eV) in the $\text{Cu}_{1.5}\text{Fe}_{1.5}\text{La}_3/\gamma\text{-Al}_2\text{O}_3$ catalyst shifted to higher BEs at 726.6, 724.6, 723.5, and 719.7 eV, respectively. The La $3d_{5/2}$ spectrum could be resolved into three main peaks, with the BEs centered at 834.5, 837.1, and 839.9 eV (Fig. 2f), assigning to La, La^{3+} , and the satellite peaks of La^{3+} in the $\text{Cu}_{1.5}\text{Fe}_{1.5}\text{La}_3/\gamma\text{-Al}_2\text{O}_3$ catalyst, respectively. After Pt addition, the positions of characteristic peaks shifted to higher BEs at 834.7, 837.4, and 840.1 eV, respectively.

In conclusion, Pt addition made the Fe 2p, Cu 2p, and La 3d peaks of the catalyst shifted to higher BEs, while the BEs of Pt 4f were lower than the corresponding standard values.³⁰ Because Fermi levels of Fe, Cu and La are lower than that of Pt, synergistic multi-metallic interaction may alter the electron cloud density around every element, leading to electron transfer and lattice expansion/compression from each of the elements Fe, Cu, and La to Pt.^{34–36} By calculating the peak areas, the Pt, Cu, Fe, and La elements in the $\text{Pt}_1\text{Cu}_1\text{Fe}_1\text{La}_3/\gamma\text{-Al}_2\text{O}_3$ catalyst mainly existed in the forms of Pt, Cu^{2+} , Cu^+ , Fe_3O_4 , and La^{3+} , along with small amounts of Pt^{2+} , Pt^{4+} , Fe^{3+} , Fe^{2+} , and La, in agreement with the XRD results.



3.2 Effects of calcination temperatures

3.2.1 Catalyst performance. The calcination temperature is known to greatly determine the catalyst properties and subsequent catalytic performance. Fig. 3 shows the catalytic behavior of the $\text{Pt}_1\text{Cu}_1\text{Fe}_1\text{La}_3/\gamma\text{-Al}_2\text{O}_3$ catalyst with 1.0 wt% Pt calcined at different temperatures. At the reaction time of 90 min, the catalyst calcined at 350 °C showed the highest catalytic activity compared with those calcined above 350 °C, along with the highest metal leaching. The high catalytic activity of this sample was partly attributed to the formation of an amorphous structure rather than a crystalline structure at low temperatures. The amorphous structure provides more surface area, more active sites, and small particle size for the improved catalytic performance. With the increase of calcination temperatures from 350 °C to 750 °C, the COD removal efficiency for the degradation of water samples decreased from 97.3% to 84.6% over the catalysts calcined at different calcination temperatures. The active metal leaching of the catalysts in water samples decreased from 5.16 mg L⁻¹ to 1.02 mg L⁻¹, indicating the improvement of the catalyst stability.

Surprisingly, the catalytic activity decreased to a large extent at temperatures above 650 °C, whereas the metal leaching was reduced. This is likely caused by the size effect or oxygen deficiency.³⁷ The $\text{Pt}_1\text{Cu}_1\text{Fe}_1\text{La}_3/\gamma\text{-Al}_2\text{O}_3$ catalyst calcined at the mid-range temperature of 650 °C showed an excellent COD removal efficiency of 94.7% for the PDW, and had total metal leaching of 1.32 mg L⁻¹ (0.09, 0.72, 0.31, 0.20 mg L⁻¹ for Pt, Cu, Fe, and La, respectively). Compared with other calcination temperatures, the $\text{Pt}_1\text{Cu}_1\text{Fe}_1\text{La}_3/\gamma\text{-Al}_2\text{O}_3$ catalyst calcined at 650 °C showed the most desirable performance, with high COD removal efficiency for the treatment of PDW, as well as low metal leaching.

To investigate the role of homogeneous phase in the CWAO process, the $\text{Pt}_1\text{Cu}_1\text{Fe}_1\text{La}_3/\gamma\text{-Al}_2\text{O}_3$ catalysts were calcined at 350 °C and 450 °C, and then mixed in the de-ionized water with vigorous stirring for 1 h at a reaction temperature of 200 °C. The catalysts were filtered through a 0.45 μm filter film to obtain solution, and methyl orange (MO) was dissolved in the resulting solution to ensure that the concentration of MO solution was 951.6 mg L⁻¹, with a COD of 2000 mg L⁻¹. Fig. S1† shows that the COD removal efficiency and the metal leaching in the MO solution. For comparison, a blank experiment with adding $\gamma\text{-Al}_2\text{O}_3$ was also performed. Compared with the blank experiment, the COD removal efficiency of leaching solution from

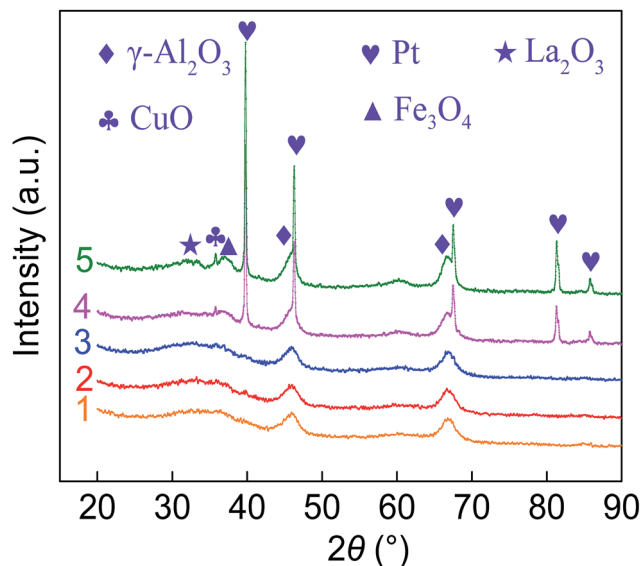


Fig. 4 XRD patterns of $\text{Pt}_1\text{Cu}_1\text{Fe}_1\text{La}_3/\gamma\text{-Al}_2\text{O}_3$ catalysts calcined at different temperatures. (1) 350 °C, (2) 450 °C, (3) 550 °C, (4) 650 °C and (5) 750 °C.

catalysts calcined at 350 °C and 450 °C increased by less than 10%, while the total level of leached metals from catalysts calcined at 350 °C and 450 °C was 5.16 mg L⁻¹ (0.27, 2.49, 1.49, 0.91 mg L⁻¹ for Pt, Cu, Fe, and La) and 3.19 mg L⁻¹ (0.13, 1.62, 1.09, 0.35 mg L⁻¹ for Pt, Cu, Fe, and La), respectively. Therefore, it is estimated that the contribution of leached metals during CWAO process over Pt-based catalysts is substantially low. Posada *et al.*³⁸ reported that the phenol was oxidized over the 4 wt% Cu/CeO₂ catalyst during the CWAO process, and homogeneous catalysis by the dissolved Cu²⁺ ions (54.5 mg L⁻¹) in the solution were partially responsible for the rapid degradation. Tu *et al.*³⁹ have studied the 2-chlorophenol was treated with the carbon-supported iron oxide catalyst in the CWAO, and 27 mg L⁻¹ of leached iron was found to play an important role in the overall CWAO performance. The use of the acetate buffer (pH = 4.5) was helpful in minimizing the iron leaching while keeping some catalytic activity. In the present study, it is found that addition of Pt in Cu-based CWAO catalyst can substantially improve the stability of catalysts while maintaining high activity towards pollutants oxidation.

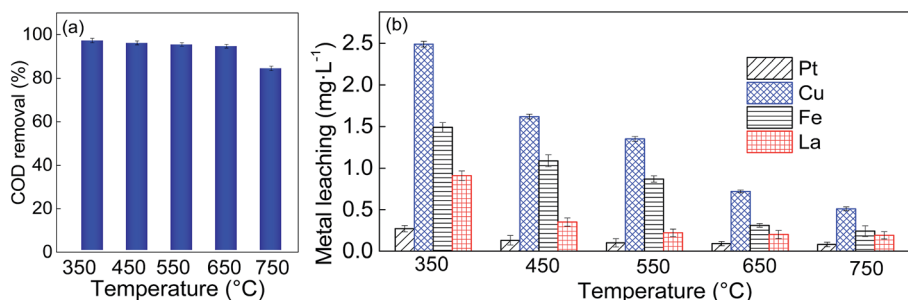


Fig. 3 Performance of $\text{Pt}_1\text{Cu}_1\text{Fe}_1\text{La}_3/\gamma\text{-Al}_2\text{O}_3$ catalysts calcined at different temperatures. (a) COD removal and (b) metal leaching.



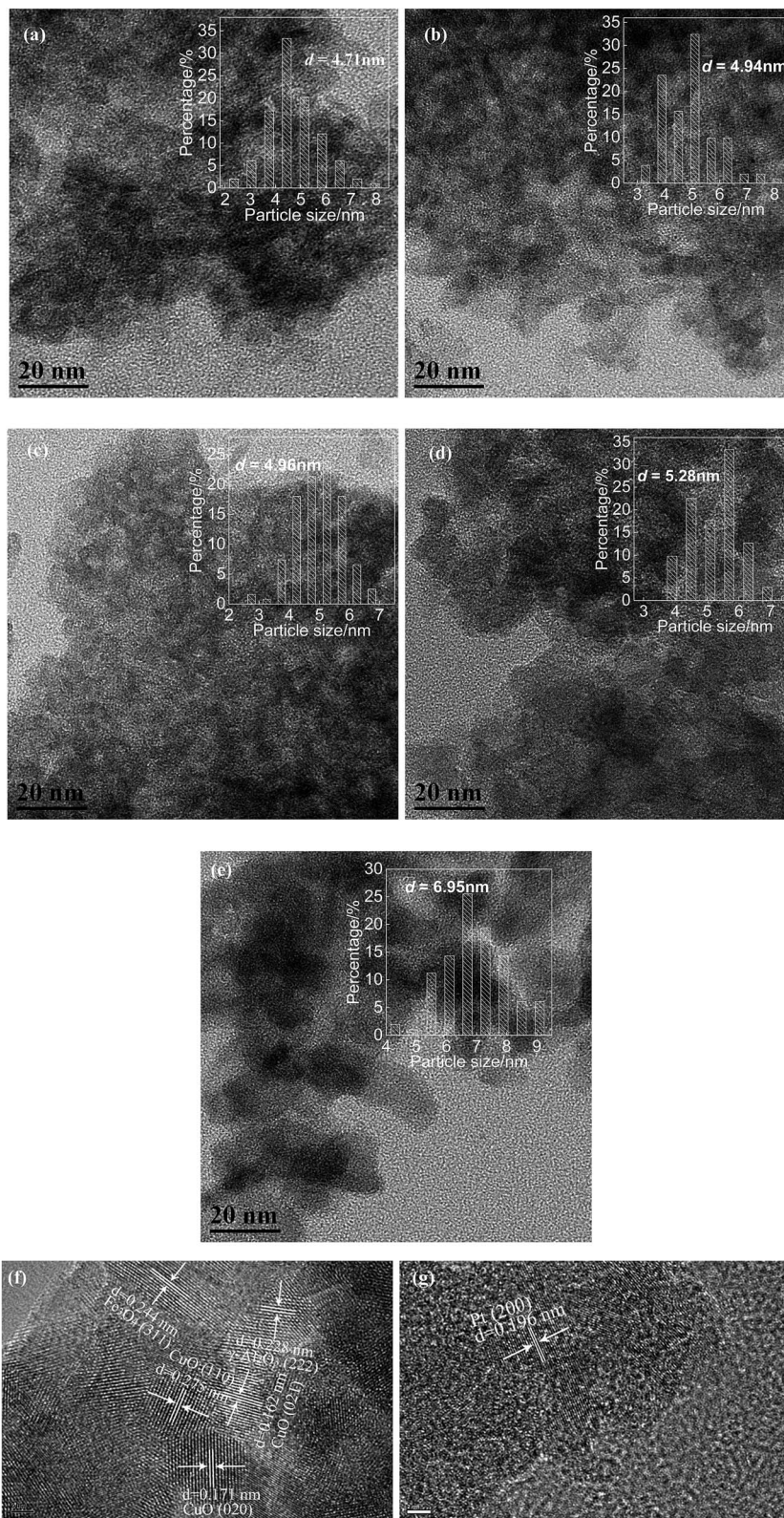


Fig. 5 HRTEM of $\text{Pt}_1\text{Cu}_1\text{Fe}_1\text{La}_3/\gamma\text{-Al}_2\text{O}_3$ catalyst obtained at (a) 350 °C, (b) 450 °C, (c) 550 °C, (d, f, g) 650 °C, (e) 750 °C.

3.2.2 XRD. In order to explore the correlation between catalytic performance and calcination temperature, the textural properties for a series of $\text{Pt}_1\text{Cu}_1\text{Fe}_1\text{La}_3/\gamma\text{-Al}_2\text{O}_3$ catalysts were

characterized by nitrogen adsorption–desorption, XRD, HRTEM, FESEM-EDS, Raman spectroscopy, and H_2 -TPR, and XPS analysis.



To investigate the crystallinity as well as the phase structure of the catalysts, XRD of the $\text{Pt}_1\text{Cu}_1\text{Fe}_1\text{La}_3/\gamma\text{-Al}_2\text{O}_3$ catalyst obtained by calcination at 350, 450, 550, 650, and 750 °C, were recorded (Fig. 4). The diffraction peaks of $\gamma\text{-Al}_2\text{O}_3$ at around 2θ of 45.9°, and 66.8° are observed for the samples at various calcination temperatures, corresponding to the (400) and (440) Bragg reflection of $\gamma\text{-Al}_2\text{O}_3$ (JCPDS 77-0396). An increase in the intensity and decrease in the peak width is observed in the XRD peaks of the catalyst components with increasing calcination temperatures, confirming the improvement of crystallinity of the tested samples. As the calcination temperature was 650 °C and above, the diffraction peaks appear at 2θ of 39.8°, 46.3°, 67.5°, 81.3°, and 85.8° corresponding to the (111), (200), (220), (311), and (222) planes, which is assigned to crystalline Pt (JCPDS 87-0646). The remaining diffraction peaks at 2θ of 35.6°, 36.8°, and 31.4° match well with their corresponding standards for CuO (JCPDS 89-5895), Fe_3O_4 (JCPDS 26-1136), and La_2O_3 (JCPDS 04-0856), respectively, representing the (-111), (311), and (400) reflection, respectively.

Therefore, the higher calcination treatment contributes to the phase transformation, but leads to a decrease in specific surface area (Table S1†). The catalyst at the calcination temperature of 350 °C exhibited the highest surface area (273.6 $\text{m}^2 \text{g}^{-1}$) and the smallest crystal size (8.2 nm), whereas the lowest surface area (196.8 $\text{m}^2 \text{g}^{-1}$) corresponds to the larger crystal size (8.7 nm) for samples obtained at 750 °C. Decreases in the pore volume and the surface area of the catalysts indicate that metals were deposited inside the pores of the support $\gamma\text{-Al}_2\text{O}_3$. As the calcination temperature was higher than 650 °C, an obvious loss of surface area was due to sintering and crystallite growth, being adverse to dispersion of catalyst particles on the surface of $\gamma\text{-Al}_2\text{O}_3$. In general, larger specific surface area of the catalyst calcined at 650 °C is favorable for dispersion stabilization of metal active phase, thus higher catalytic activity and the stability of the catalyst.

3.2.3 Catalyst morphology. Fig. 5 presents the HRTEM images for the $\text{Pt}_1\text{Cu}_1\text{Fe}_1\text{La}_3/\gamma\text{-Al}_2\text{O}_3$ catalyst calcined at different temperatures. By calculating the sizes of about 100 particles, the particle size distribution histogram of the $\text{Pt}_1\text{Cu}_1\text{Fe}_1\text{La}_3/\gamma\text{-Al}_2\text{O}_3$ catalyst is obtained, as shown in Fig. 5a–e. The average particle size varies from 4.71–6.95 nm with the elevation of calcination temperatures, due to the particle growth and enrichment of metallic oxide species over the surface upon calcination. Interestingly, at calcination temperatures above 650 °C, the particle size of the catalyst becomes more larger, corresponding to a significant decrease in their catalytic performance (Fig. 3). In the case of the $\text{Pt}_1\text{Cu}_1\text{Fe}_1\text{La}_3/\gamma\text{-Al}_2\text{O}_3$ catalyst calcined at 650 °C, the lattice fringes of metallic oxide can be clearly seen in the HRTEM images of the catalysts (Fig. 5f). The lattice spacing of 0.228 nm is assigned to the (111) interlayer spacing of $\gamma\text{-Al}_2\text{O}_3$, and 0.244 nm lattice spacing matches well with that of the (311) planes of Fe_3O_4 . In addition, the observed lattice spacing of 0.275 nm, 0.171 nm, and 0.162 nm is assigned to the (110), (020), and (021) plane of CuO, respectively. As seen from the other picture, the lattice spacing of 0.196 nm is assigned to the (200) interlayer spacing of Pt in Fig. 5g. These observations are also consistent with XRD results. SEM-EDS analysis indicates that $\text{Pt}_1\text{Cu}_1\text{Fe}_1\text{La}_3/\gamma\text{-Al}_2\text{O}_3$

catalyst calcined at 650 °C has flakes or quasi-spheres porous structure (Fig. S2a†). Pt, Cu, Fe, and La elements are highly dispersed in the $\gamma\text{-Al}_2\text{O}_3$ support, and the weight ratio of Pt, Cu, Fe, and La is 0.79 : 0.78 : 0.81 : 2.41, approximate to the theoretical value of 1 : 1 : 1 : 3 (Fig. S2b and S3†).

3.2.4 Raman. Raman spectroscopy of $\text{Pt}_1\text{Cu}_1\text{Fe}_1\text{La}_3/\gamma\text{-Al}_2\text{O}_3$ catalysts calcined at different temperatures were recorded in the 200–1200 cm^{-1} region. Fig. 6 shows the characteristic broadening and softening effects at high temperature. It is known that the $\gamma\text{-Al}_2\text{O}_3$ support has no Raman active modes.⁴⁰ The peaks centred at 580 and 692 cm^{-1} are the characteristic spectra of the magnetite. A narrow band observed at about 1041 cm^{-1} is assigned to siderite.⁴¹ When the calcination temperatures are over 650 °C, a band at about 1041 cm^{-1} disappears in the spectra, confirming that the siderite phase has changed. Owing to calcination and sintering of catalyst NPs, two prominent bands centred at 222 and 289 cm^{-1} which are the vibration modes of Fe–O bonds of Fe_3O_4 nanoparticles, move towards a lower Raman shift. The peaks at 399 cm^{-1} is assigned to the E_g modes. The peak at 285 cm^{-1} and peaks at 341 and 614 cm^{-1} are assigned to the A_g mode and B_g modes of CuO. Xu *et al.*⁴² reported that a series of CuO samples annealed in air at various temperatures with different grain sizes. When the grain size increases, the Raman spectral peaks were found at 295, 342 and 628 cm^{-1} , and the wavenumbers with the three $A_g + 2B_g$ modes are lower than those reported in the literature (298, 345 and 632 cm^{-1}) due to size effects. With an increase of the calcination temperatures, the grain size of the obtained samples increases in our manuscript, resulting that the Raman spectral peaks slightly trend to red shift and become much weaker and broader. Wavenumbers of these peaks are lower than those reported in the literature due to size effects, in line with XRD data (Fig. 4) and HRTEM results (Fig. 5). Raman bands of La_2O_3 are not observed in the $\text{Pt}_1\text{Cu}_1\text{Fe}_1\text{La}_3/\gamma\text{-Al}_2\text{O}_3$ samples, confirming the presence of lanthanum in a disperse phase on the catalyst.⁴³ There are no Raman peaks for Pt monatomic molecules because of no vibration and rotational degrees of freedom.

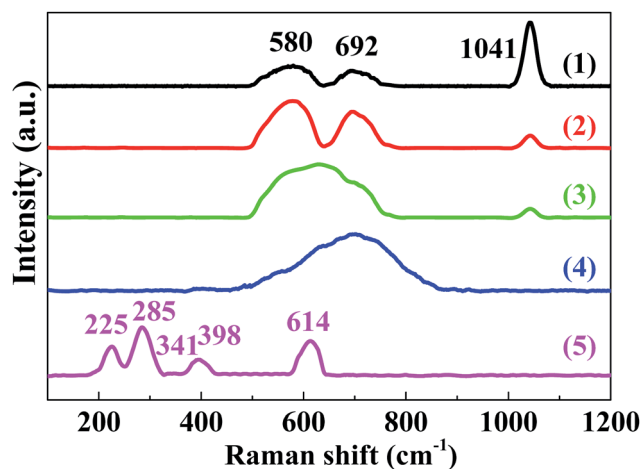


Fig. 6 Raman spectroscopy of $\text{Pt}_1\text{Cu}_1\text{Fe}_1\text{La}_3/\gamma\text{-Al}_2\text{O}_3$ catalysts calcined at different temperatures. (1) 350 °C, (2) 450 °C, (3) 550 °C, (4) 650 °C and (5) 750 °C.



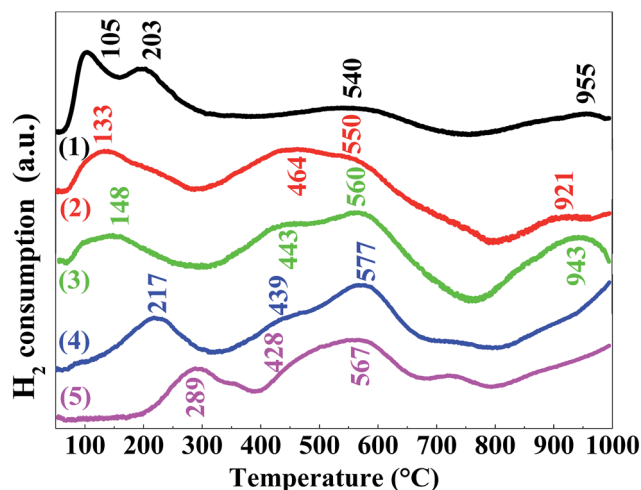


Fig. 7 H_2 -TPR profiles of $Pt_1Cu_1Fe_1La_3/\gamma-Al_2O_3$ catalysts calcined at different temperatures. (1) 350 °C, (2) 450 °C, (3) 550 °C, (4) 650 °C and (5) 750 °C.

3.2.5 H_2 -TPR. Generally, the reducibility of metal species provides useful information about the structure and nature of a particular catalyst. The H_2 -TPR experiment was therefore conducted to understand the redox properties over the $Pt_1Cu_1Fe_1La_3/\gamma-Al_2O_3$ samples annealed at the different temperatures. As shown in Fig. 7, the $Pt_1Cu_1Fe_1La_3/\gamma-Al_2O_3$ sample normally shows four-steps reductions within the temperature range from 50 to 1000 °C. As previously reported, the $\gamma-Al_2O_3$ support cannot be reduced (data not shown).⁴⁴ The first peaks at 105–289 °C may be attributed to the reduction of surface oxygen, hydroxyl species and both PtO and PtO₂ species.^{45,46} The peaks at 418–464 °C and 540–577 °C are related to the reduction of Cu and Fe (*i.e.* CuO → Cu₂O → Cu and Fe₂O₃ → Fe₃O₄ → FeO →

Fe), respectively.^{47–51} The high temperature reduction peaks at 921–955 °C can be assigned to the reduction of La₂O₃.⁵² It should be noted that the intensity of the first reduction peak decreases as the calcination temperature increases, implying the loss of surface oxygen and OH groups or reduction of PtO and PtO₂. This is in good agreement with XRD results which show the improved crystallinity and presence of elemental Pt at elevated calcination temperature (Fig. 4).

3.3 Catalyst reusability

To be cost-effective, an ideal CWAQ catalyst should show sufficient activity upon repeated use. Thus, the reusability of the $Pt_1Cu_1Fe_1La_3/\gamma-Al_2O_3$ catalyst was evaluated in CWAQ of PDW. The used catalyst was washed with deionized water and then dried at 105 °C for 10 h. Then it was reused in the next cycle without any calcinations treatment. As shown in Fig. 8, the high COD removal efficiency and decolorization rate for PDW still maintain after five cycles, indicating that $Pt_1Cu_1Fe_1La_3/\gamma-Al_2O_3$ is a promising catalyst with high activity and stability.

4 Conclusions

A novel $Pt_1Cu_1Fe_1La_3/\gamma-Al_2O_3$ catalyst with 1.0 wt% Pt was prepared by the incipient-wetness impregnation method, and applied in the CWAQ of PDW. Compared with the $Cu_{1.5}Fe_{1.5}La_3/\gamma-Al_2O_3$ catalyst, the COD removal efficiency for the $Pt_1Cu_1Fe_1La_3/\gamma-Al_2O_3$ catalyst increases from 68.8% to 94.7%, and the decolorization rate increases from 98.8% to 99.5%, whereas the total metal leaching dramatic decreases from 6.43 to 1.32 mg L⁻¹. These results indicate that the activity and stability of the Pt-modified catalyst are improved significantly due to the oxygen deficiency and the size effect. With increasing calcination temperatures, the catalytic activity decreases due to reduced specific surface area and lower pore volume of the catalyst. Simultaneously, the stability of the catalyst increases at higher calcination temperatures as reflected in decreased metal leaching due to higher degree of crystallinity in the samples. The XRD, HRTEM and XPS results indicate that the $Pt_1Cu_1Fe_1La_3/\gamma-Al_2O_3$ catalyst existed as a composite mixture of mainly Pt, CuO, Fe₃O₄, and La₂O₃. $Pt_1Cu_1Fe_1La_3/\gamma-Al_2O_3$ catalyst exhibits excellent reusability. For five runs of sample treatment, the recycled catalyst shows no significant loss of activity. Thus, this new Pt-modified catalyst is a promising candidate for PDW treatment using the CWAQ method.

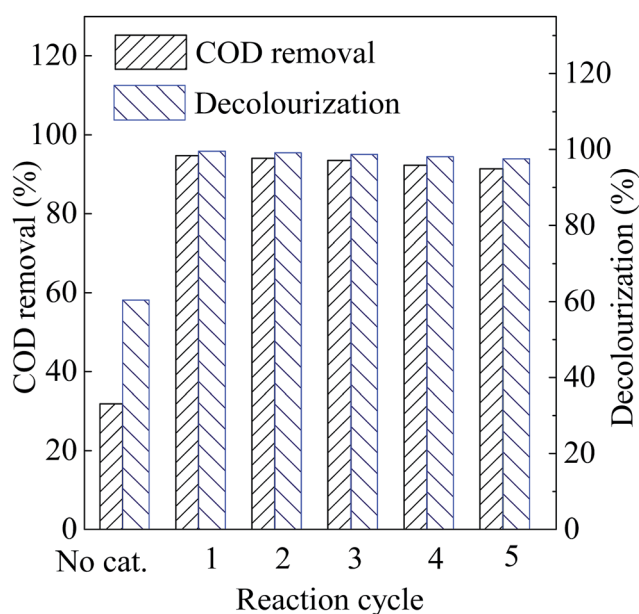


Fig. 8 Recyclability of $Pt_1Cu_1Fe_1La_3/\gamma-Al_2O_3$ catalyst.

Conflicts of interest

There are no conflicts to declare.

Acknowledgements

This work was supported by the 2016 Foshan Science and Technology Project (2016GA10159), the Natural Science Foundation of Guangdong Province (2014A030312007) and the China Postdoctoral Science Foundation (2014M552202).



References

- 1 A. K. An, J. Guo, S. Jeong, E. J. Lee, S. A. Tabatabai and T. Leiknes, *Water Res.*, 2016, **103**, 362–371.
- 2 H. Rong, B. Gao, R. Li, Y. Wang, Q. Yue and Q. Li, *Chem. Eng. J.*, 2014, **243**, 169–175.
- 3 A. Paz, J. Carballo, M. J. Perez and J. M. Dominguez, *Chemosphere*, 2017, **181**, 168–177.
- 4 E. Brillas and C. A. Martínez-Huitle, *Appl. Catal., B*, 2015, **166–167**, 603–643.
- 5 R. Huang, Y. Liu, Z. Chen, D. Pan, Z. Li, M. Wu, C. H. Shek, C. M. Wu and J. K. Lai, *ACS Appl. Mater. Interfaces*, 2015, **7**, 3949–3959.
- 6 Z. Guerra-Que, G. Torres-Torres, H. Pérez-Vidal, I. Cuauhtémoc-López, A. Espinosa de los Monteros, J. N. Beltramini and D. M. Frías-Márquez, *RSC Adv.*, 2017, **7**, 3599–3610.
- 7 Y. Zhang, Z. Zhang, Q. Yan and Q. Wang, *Appl. Catal., A*, 2016, **511**, 47–58.
- 8 D. K. Mondal, C. Mondal and S. Roy, *RSC Adv.*, 2016, **6**, 114383–114395.
- 9 C. Ma, Y. Wen, Q. Yue, A. Li, J. Fu, N. Zhang, H. Gai, J. Zheng and B. H. Chen, *RSC Adv.*, 2017, **7**, 27079–27088.
- 10 D. Wu, Z. Hu, X. Zhang, C. Zhang, K. Sun and S. Lu, *RSC Adv.*, 2017, **7**, 37487–37494.
- 11 I. Benhamed, L. Barthe, R. Kessas, C. Julcour and H. Delmas, *Appl. Catal., B*, 2016, **187**, 228–237.
- 12 D. Xu, F. Cheng, Q. Lu and P. Dai, *Ind. Eng. Chem. Res.*, 2014, **53**, 2625–2632.
- 13 Z. Wang, L. Ai, Y. Huang, J. Zhang, S. Li, J. Chen and F. Yang, *RSC Adv.*, 2017, **7**, 30941–30948.
- 14 Y. Zhao, X. Zhou, Y. Ding, J. Huang, M. Zheng and W. Ye, *J. Catal.*, 2016, **338**, 30–37.
- 15 M. Gutierrez-Arzaluz, L. Norena-Franco, S. Angel-Cuevas, V. Mugica-Alvarez and M. Torres-Rodriguez, *Molecules*, 2016, **21**, 668.
- 16 J. T. Mefford, W. G. Hardin, S. Dai, K. P. Johnston and K. J. Stevenson, *Nat. Mater.*, 2014, **13**, 726–732.
- 17 Y. Zhu, C. Gao, Q. Han, Z. Wang, Y. Wang, H. Zheng and M. Wu, *J. Catal.*, 2017, **346**, 62–69.
- 18 M. Nesselberger, M. Roefzaad, R. F. Hamou, P. U. Biedermann, F. F. Schweinberger, S. Kunz, K. Schloegl, G. K. Wiberg, S. Ashton, U. Heiz, K. J. Mayrhofer and M. Arenz, *Nat. Mater.*, 2013, **12**, 919–924.
- 19 S. Sui, X. Wang, X. Zhou, Y. Su, S. Riffat and C. Liu, *J. Mater. Chem. A*, 2017, **5**, 1808–1825.
- 20 L. Phuong Thu and B. Michele, *J. Hazard. Mater.*, 2016, **310**, 108–116.
- 21 E. Szabados, G. Sági, F. Somodi, B. Maróti, D. Srankó and A. Tungler, *J. Ind. Eng. Chem.*, 2017, **46**, 364–372.
- 22 Sushma and A. K. Saroha, *J. Cleaner Prod.*, 2017, **162**, 973–981.
- 23 M. A. L. Rocha, G. Del Ángel, G. Torres-Torres, A. Cervantes, A. Vázquez, A. Arrieta and J. N. Beltramini, *Catal. Today*, 2015, **250**, 145–154.
- 24 A. E. D. L. Monteros, G. Lafaye, A. Cervantes, G. Del Angel, J. Barbier Jr and G. Torres, *Catal. Today*, 2015, **258**, 564–569.
- 25 C. Lousteau, M. Besson and C. Descorme, *Catal. Today*, 2015, **241**, 80–85.
- 26 S. Morales-Torres, A. M. T. Silva, F. J. Maldonado-Hódar, B. F. Machado, A. F. Pérez-Cadenas, J. L. Faria, J. L. Figueiredo and F. Carrasco-Marin, *Appl. Catal., B*, 2011, **105**, 86–94.
- 27 S. Keav, A. E. de los Monteros, J. Barbier and D. Duprez, *Appl. Catal., B*, 2014, **150–151**, 402–410.
- 28 Y. Zhang, F. Peng and Y. Zhou, *Chin. J. Chem. Eng.*, 2016, **24**, 1171–1177.
- 29 N. Jaafarzadeh, F. Ghanbari, M. Ahmadi and M. Omidinasab, *Chem. Eng. J.*, 2017, **308**, 142–150.
- 30 K. S. Kim, N. Winograd and R. E. Davis, *J. Am. Chem. Soc.*, 1971, **93**, 6296–6297.
- 31 X. Zhu, S. Zhang, Y. Yang, C. Zheng, J. Zhou, X. Gao and X. Tu, *Appl. Catal., B*, 2017, **213**, 97–105.
- 32 Y. Zheng, K. Li, H. Wang, D. Tian, Y. Wang, X. Zhu, Y. Wei, M. Zheng and Y. Luo, *Appl. Catal., B*, 2017, **202**, 51–63.
- 33 L. Zhu, J. Wang, S. Rong, H. Wang and P. Zhang, *Appl. Catal., B*, 2017, **211**, 212–221.
- 34 Y. Wang, H. Arandiyán, J. Scott, A. Bagheri, H. Dai and R. Amal, *J. Mater. Chem. A*, 2017, **5**, 8825–8846.
- 35 H. Wu, G. Pantaleo, V. La Parola, A. M. Venezia, X. Collard, C. Aprile and L. F. Liotta, *Appl. Catal., B*, 2014, **156–157**, 350–361.
- 36 R. Matarrese, S. Morandi, L. Castoldi, P. Villa and L. Lietti, *Appl. Catal., B*, 2017, **201**, 318–330.
- 37 J. A. Onrubia, B. Pereda-Ayo, U. De-La-Torre and J. R. González-Velasco, *Appl. Catal., B*, 2017, **213**, 198–210.
- 38 D. Posada, P. Betancourt, F. Liendo and J. L. Brito, *Catal. Lett.*, 2006, **106**, 81–88.
- 39 Y. Tu, Y. Xiong, S. Tian, L. Kong and C. Descorme, *J. Hazard. Mater.*, 2014, **276**, 88–96.
- 40 X. Wu, L. Zhang, D. Weng, S. Liu, Z. Si and J. Fan, *J. Hazard. Mater.*, 2012, **225–226**, 146–154.
- 41 D. Neff, S. Reguer, L. Bellot-Gurlet, P. Dillmann and R. Bertholon, *J. Raman Spectrosc.*, 2004, **35**, 739–745.
- 42 J. Xu, W. Ji, Z. Shen, W. Li, S. Tang, X. Ye, D. Jia and X. Xin, *J. Raman Spectrosc.*, 1999, **30**, 413–415.
- 43 K. Villa, S. Murcia-López, J. R. Morante and T. Andreu, *Appl. Catal., B*, 2016, **187**, 30–36.
- 44 S. García-Fernández, I. Gandarias, J. Requies, M. B. Güemez, S. Bennici, A. Auroux and P. L. Arias, *J. Catal.*, 2015, **323**, 65–75.
- 45 B. Chen, X. Zhu, M. Crocker, Y. Wang and C. Shi, *Appl. Catal., B*, 2014, **154–155**, 73–81.
- 46 S. Liu, J. Ren, S. Zhu, H. Zhang, E. Lv, J. Xu and Y.-W. Li, *J. Catal.*, 2015, **330**, 485–496.
- 47 S. Gomez, L. Lericci, C. Saux, A. L. Perez, C. D. Brondino, L. Pierella and L. Pizzio, *Appl. Catal., B*, 2017, **202**, 580–586.
- 48 J. L. Santos, T. R. Reina, S. Ivanova, M. A. Centeno and J. A. Odriozola, *Appl. Catal., B*, 2017, **201**, 310–317.



- 49 J. Li, P. Ye, J. Fang, M. Wang, D. Wu, A. Xu and X. Li, *Appl. Surf. Sci.*, 2017, **422**, 754–762.
- 50 M. Albrecht, U. Rodemerck, M. Schneider, M. Bröring, D. Baabe and E. V. Kondratenko, *Appl. Catal., B*, 2017, **204**, 119–126.
- 51 M. Romero-Sález, D. Divakar, A. Aranzabal, J. R. González-Velasco and J. A. González-Marcos, *Appl. Catal., B*, 2016, **180**, 210–218.
- 52 X. Zheng, H. Lin, J. Zheng, X. Duan and Y. Yuan, *ACS Catal.*, 2013, **3**, 2738–2749.

